Lowest accreting protoplanetary discs as diagnostic of disc dispersal

Barbara Ercolano,[1,2]★ Giovanni Picogna[1] and Kristina Monsch[3]
[1] University Observatory, Faculty of Physics, Ludwig-Maximilians-Universität München, Scheinerstr. 1, 81679 Munich, Germany
[2] Exzellenzcluster 'Origins', Boltzmannstr. 2, 85748 Garching, Germany
[3] Harvard-Smithsonian Center for Astrophysics, 60 Garden Street, Cambridge MA 02138, USA

Accepted XXX. Received YYY; in original form ZZZ

ABSTRACT

Photoevaporation from high energy stellar radiation has been thought to drive the dispersal of protoplanetary discs. Different theoretical models have been proposed, but their predictions diverge in terms of the rate and modality at which disc lose their mass, with significant implications for the formation and evolution of planets. In this letter we use disc population synthesis models to interpret recent observations of the lowest accreting protoplanetary discs, comparing predictions from EUV-driven and X-ray driven photoevaporation models. We show that the recent data point to X-ray photoevaporation as the preferred mechanism driving the final stages of protoplanetary disc dispersal.

Key words: keyword1 – keyword2 – keyword3

1 INTRODUCTION

Circumstellar disks are studied since more than 40 years, though the mechanism responsible for their evolution and final dispersal remains elusive (see for recent reviews Pascucci et al. 2022; Lesur et al. 2022). It has been determined observationally that the disc fraction of accreting pre-main-sequence stars decreases with the age of the population (see e.g. Mamajek 2009), while having $\sim 10\%$ of non-accreting star bearing discs (Skrutskie et al. 1990).

The transition between accreting and non-accreting stars plays an important role in determining the final architecture of the forming planetary systems, as the speed of this process can cut out the supply for forming giant planets and halt their migration (see e.g. Monsch et al. 2019).

Thanathibodee et al. (2022) recently looked for an accretion signatures in disc-bearing stars previously thought to be non-accretors, using the He I λ10830Å line. This high excitation line allowed them to probe material in the innermost regions of protostellar discs, possibly detecting accretion streamers. They found that a large fraction of this sample (at least $20-30\%$) indeed shows signs of accretion via strong red-shifted absorption consistent with free-fall velocities, preferentially at young ages and almost independently of the stellar mass. The accretion rates were then determined independently by fitting the H-α profiles, of a sub-sample of these stars, using magnetospheric accretion models (Thanathibodee et al. 2023). Interestingly, although the statistics was very low (24 sources), the authors derived a minimum accretion rate of the order of 10^{-10} $M_\odot$ yr^{-1}, even though their method was able to detect rates 5 to 10 times lower, hinting some physical rather than selection limit. They further suggested that, since this rate is similar to the mass-loss rate provided by classical models of EUV photoevaporation (see e.g. Alexander & Armitage 2007), this mechanism of disc dispersal is a viable candidate to explain the transition between an accreting and non-accreting disc.

In this paper we test this hypothesis by producing synthetic populations of viscously evolving discs dispersed by photoevaporation, testing the different scenarios of EUV- and X-ray photoevaporation.

In Section 2 we describe the method adopted, and in Section 3 we present the result and draw the conclusions in Section 4.

2 METHODS

We use the one-dimensional viscous evolution code SPOCK (Ercolano & Rosotti 2015) which evolves the gas following

$$\frac{\partial \Sigma}{\partial t} = \frac{1}{R}\frac{\partial}{\partial R}\left[3R^{1/2}\frac{\partial}{\partial R}(\nu\Sigma R^{1/2})\right] - \dot{\Sigma}_w(R,t)\,, \tag{1}$$

where the first term on the right hand side describes the viscous disc evolution (Lynden-Bell & Pringle 1974), and the second one is a sink term modelling the mass-loss due to internal disc photoevaporation.

We consider either an EUV or X-ray mass-loss rate internal photoevaporation profiles as they are well-studied in literature, and simple 1D presciptions of the disc mass-loss rates are provided.

2.1 X-ray photoevaporation

The XEUV surface mass-loss rate is given following Picogna et al. (2019)

$$\begin{aligned}\dot{\Sigma}_{\rm XEUV}(R) &= \ln(10)\left(\frac{6a\,\ln(R)^5}{R\,\ln(10)^6} + \frac{5b\,\ln(R)^4}{R\,\ln(10)^5} + \frac{4c\,\ln(R)^3}{R\,\ln(10)^4} + \right.\\ &\quad \frac{3d\,\ln(R)^2}{R\,\ln(10)^3} + \frac{2e\,\ln(R)}{R\,\ln(10)^2} + \\ &\quad \left.\frac{f}{R\,\ln(10)}\right)\frac{\dot{M}_{\rm XEUV}(R)}{2\pi R}\,,\end{aligned} \tag{2}$$

★ E-mail: ercolano@usm.lmu.de

where

$$\frac{\dot{M}_{\rm XEUV}(R)}{\dot{M}_{\rm XEUV}(M_\star, L_{X,\rm soft})} = 10^{a \log R^6 + b \log R^5 + c \log R^4 + d \log R^3 + e \log R^2 + f \log R + g} \tag{3}$$

and the parameters for the different stellar masses are given in Table 1. The mass-loss rate as a function of X-ray luminosity and stellar mass is given by (Ercolano et al. 2021; Picogna et al. 2021)

$$\dot{M}_{\rm XEUV}(M_\star, L_{X,\rm soft}) = \dot{M}_{\rm XEUV}(M_\star) \frac{\dot{M}_{\rm XEUV}(L_{X,\rm soft})}{\dot{M}_{\rm XEUV}(L_{X,\rm soft,mean})}, \tag{4}$$

where the mass-loss rate as a function of stellar mass is

$$\dot{M}_{\rm XEUV}(M_\star) = 3.93 \times 10^{-8} \left(\frac{M_\star}{M_\odot}\right) \tag{5}$$

and the dependance on the soft component of the X-ray luminosity is given by

$$\dot{M}_{\rm XEUV}(L_{X,\rm soft}) = 10^{a_L \exp\left(\frac{(\ln(\log(L_{X,\rm soft}) - b_L)^2}{c_L}\right) + d_L}, \tag{6}$$

where $a_L = -1.947 \cdot 10^{17}$, $b_L = -1.572 \cdot 10^{-4}$, $c_L = -0.2866$, $d_L = -6.694$, the soft component of the X-ray luminosity is given by

$$L_{X,\rm soft} = 10^{0.95 \log(L_X) + 1.19}, \tag{7}$$

and the mean component of the X-ray luminosity $L_{X,\rm soft,mean}$ is the soft X-ray luminosity of a star with a total X-ray luminosity given by the observational relation between stellar mass and X-ray luminosity (see eq. 17, Güdel et al. 2007).

2.2 EUV photoevaporation

We divided the EUV surface mass-loss rate in its diffuse and direct components following Alexander & Armitage (2007)

$$\dot{\Sigma}_{\rm EUV}(R) = \dot{\Sigma}_{\rm diffuse}(R) + \dot{\Sigma}_{\rm direct}(R,t) \cdot f(R), \tag{8}$$

where $f(R) = 1 + \exp(-\frac{R - R_{\rm in}}{H_{\rm in}})$ is a smoothing function to avoid numerical problems close to the disc inner edge, $R_{\rm in}(t)$ is the radius of the inner disc edge, $H_{\rm in}(t)$ is the disc scale height at the inner edge.

The diffuse component of the EUV surface mass-loss rate is then given by

$$\dot{\Sigma}_{\rm diffuse}(R) = 2 n_0(R) u_l(R) \mu m_H \qquad \text{for } R \geq 0.1 R_g, \tag{9}$$

where the density at the base of the flow is

$$n_0(R) = C_1 \left(\frac{3\Phi_{\rm diff}}{4\pi\alpha_B R_g^3}\right)^{1/2} \left(\frac{2}{(R/R_g)^{15/2} + (R/R_g)^{25/2}}\right)^{1/5}, \tag{10}$$

the wind launch velocity

$$u_l(R) = c_s A \exp\left[B\left(\frac{R}{R_g} - 0.1\right)\right]\left(\frac{R}{R_g} - 0.1\right)^D, \tag{11}$$

$\mu = 1.35$ the mean molecular weight of the ionized gas, m_H the mass of a hydrogen atom, $C_1 \simeq 0.14$, R_g the gravitational radius, $\alpha_B = 2.6 \cdot 10^{-13}$ is the Case B recombination coefficient for atomic hydrogen at 10^4 K, $c_s = 10$ km s^{-1} the sound speed of the ionized gas, $A = 0.3423$, $B = 0.3612$, $D = 0.2457$, and the stellar diffuse ionizing EUV flux

$$\Phi_{\rm diff} = \begin{cases} \Phi_{\rm EUV}\left(\frac{R_{\rm thin}}{R_{\rm in}}\right) & \text{if } R_{\rm thin} < R_{\rm crit}, \\ \Phi_{\rm EUV} & \text{otherwise,} \end{cases} \tag{12}$$

where $\Phi_{\rm EUV}$ is the unattenuated stellar ionizing EUV flux (in photons s^{-1}), $R_{\rm thin}$ is the radius at which the disc becomes optically thin in the vertical direction

$$\Sigma_g(R_{\rm thin}) = m_H \sigma_{13.6\,\rm eV}^{-1}, \tag{13}$$

$\sigma_{13.6\,\rm eV} = 6.3 \cdot 10^{-18}$ cm^2 is the absorption cross-section for ionizing photons, $R_{\rm crit}$ is the critical radius at which the gap opens

$$R_{\rm crit} = 1.4 \left(\frac{M_\star}{M_\odot}\right) \text{ au}. \tag{14}$$

The direct component of the EUV surface mass-loss rate (defined only for $R > R_{\rm in}$) is given by

$$\dot{\Sigma}_{\rm direct}(R,t) = 2C_2 \mu m_H c_s \left[\frac{\Phi_{\rm EUV}}{4\pi\alpha_B (H/R) R_{\rm in}^3(t)}\right]^{1/2} \left[\frac{R}{R_{\rm in}(t)}\right]^{-a}, \tag{15}$$

where $C_2 = 0.235$, $a = 2.42$, H/R is the disc aspect ratio.

2.3 Population synthesis

We assume a initial stellar mass function following Kroupa (2001)

$$\xi(m) \propto m^{-\alpha}, \tag{16}$$

where $\alpha = 1.3 \pm 0.5$ for $0.08 \leq m/M_\odot < 0.5$ and $\alpha = 2.3 \pm 0.3$ for $0.5 \leq m/M_\odot \leq 1$, from which we obtain the distribution shown in Figure 1 (panel a) for a sample of 10,000 stars. The adopted weighting of the distribution based on eq. 16 is marked with a dashed red line, and the median stellar mass value given by the dotted dashed red line is ~ 0.3 M$_\odot$.

Güdel et al. (2007) derived an observational relation between the median X-ray luminosities and stellar masses

$$\log_{10}(L_X) = (1.54 \pm 0.12) \log_{10}(M_\star) + (30.31 \mp 0.06), \tag{17}$$

though a large spread is observed around the mean values, which becomes larger for small mass stars (e.g. Getman et al. 2022). Kuhn & Hillenbrand (2019) took a subsample of the Chandra Orion Ultradeep Project (COUP, Feigelson et al. (2005); Getman et al. (2005)) and stratified it in 3 stellar mass bins using the Baraffe et al. (1998) evolutionary models. From this sample one can derive a X-ray luminosity function (XLF) as a function of stellar mass. We then calculated the median stellar mass for the three stellar mass bins given the adopted IMF, and shifted the XLF distribution to match the given value of the stellar mass. We sampled then the X-ray luminosity given the probability density corrected for the stellar mass and obtained the X-ray luminosity distribution shown in Figure 1 (panel b) from the 10,000 sampled stellar masses, with a median value of $10^{29.4}$ erg s^{-1} and a spread over 4 orders of magnitude.

The EUV rates are shown to scale with the ratio of incoming ionising flux. However, there is no clear evidence on the origin of the EUV flux. Assuming that the EUV flux has the same origin as the X-ray flux we can then adopt the same scaling relation as eq. 17

$$\log_{10}(\Phi_{EUV}) = 1.54 \log_{10}(M_\star) + 42 \tag{18}$$

and adopt a small dispersion around the mean value for each stellar mass of 0.25 dex, as shown in Figure 1 (panel c), which gives a range of ionizing flux from $10^{40} s^{-1}$ to $10^{42.5} s^{-1}$ and a median value of $10^{41.2} s^{-1}$.

We constrained the disc properties in order to match the observed mean disc lifetime of 2-3 Myr (see e.g. Ribas et al. 2014). For the EUV profile we sampled the viscous α and scaling radius R_1 for disc

Table 1. Parameters for the Surface density profiles in equations 2,3

$M_\star$ [$M_\odot$]	a	b	c	d	e	f	g	$\dot{M}_w$
1.0	−0.6344	6.3587	−26.1445	56.4477	−67.7403	43.9212	−13.2316	3.86446
0.5	−1.2320	10.8505	−38.6939	71.2489	−71.4279	37.8707	−9.3508	1.9046
0.3	−1.3206	13.0475	−53.6990	117.6027	−144.3769	94.7854	−26.7363	1.17156
0.1	−3.8337	22.9100	−55.1282	67.8919	−45.0138	16.2977	−3.5426	0.37588

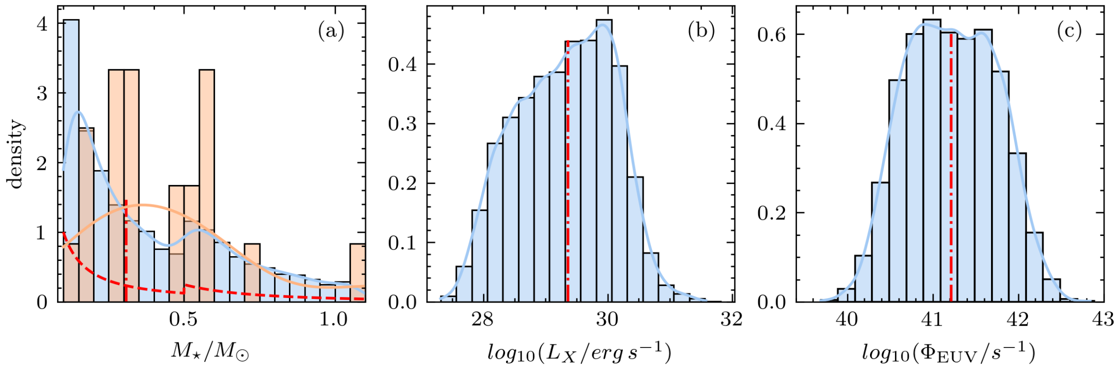

Figure 1. Panel a: histogram of the stellar mass distribution in our population synthesis, where the KDE is overplotted with a blue solid line, the median value of 0.3 $M_\odot$ is marked with a dotted-dashed red line, and the adopted weigthing based on the Kroupa IMF is plotted with a dashed red line. Panel b: histogram of the X-ray luminosity density distribution in the XEUV population synthesis, where the KDE is overplotted with a blue solid line and the median value of 29.4 is marked with a dotted dashed red line. Panel c: histogram of the ionizing flux density distribution in the EUV population synthesis, where the KDE is overplotted with a blue solid line and the median value of 41.2 is marked with a dotted dashed red line.

masses ranging from 0.1 to $0.01 M_\star$ for a typical star with median values from our distribution ($M_\star = 0.3 M_\odot$, $\Phi_{\rm EUV} = 10^{41.2}$ s^{-1}) and then we selected only the ones that were giving a correct disc life-time and obtained a best linear fit given by:

$$R_1 = 60.4\alpha + 3009.7 M_d [M_\star] + 226.6 \qquad [\text{au}] . \tag{19}$$

We then sampled the whole stellar mass range and obtained the full sampling of the parameter space. For the XEUV profile we realized that the disc evolution was primarily driven by the internal photoevaporation rather than the disc properties, thus we chose to sample uniformly the parameter space for the disc properties and fix only the disc mass to $0.1 M_\star$ as this is a reasonable value of the initial disc mass when the disc self-gravity stops being the driver of disc evolution and the approximation of a viscously evolving disc is reasonable. We summarize the parameter space probed in Table 2.

3 RESULTS

Figure 2 shows the accretion rates as a function of time for a population synthesis of 10,000 discs sampled as described in the previous section. Overplotted with dots of variable size (based on their stellar mass) is the population of low accretors from Thanathibodee et al. (2023), and the observational limit of the He I λ10830 marked with a black dashed line at 10^{-11} $M_\odot$ yr^{-1}. One can immediately see that while the XEUV profile catches all the observed data points in the region with high density ($> 10^{-2}$), the EUV cannot explain the data for the older star-forming regions (Orion OB1a and Upper Sco). Furthermore the observational data points lie in the upper region of the distribution, even though they are a sample of the low-accretors population. This means that the bulk of the discs in the studied star forming regions covers a region not explained by the EUV photoevaporation profiles.

Small mass stars (small dots) cover the lower part of the high density distribution while bigger stars the top part. This is expected from the observationally derived relation between accretion rate and stellar masses, that shows a sharp increase of the accretion rate as a function of stellar mass with a broken power law (Alcalá et al. 2017).

We plotted in Figure 3 the histogram of the accretion rate distribution for the EUV (in blue) and XEUV (in orange) populations. We overplotted as well the median accretion rates in dotted-dashed blue and orange line respectively, and the median accretion rate for the observed population of low-accretors with a dotted-dashed black line. From this one can directly visualize how the median of the XEUV population and the observed low-accretors is very similar, while it is close to the high-accretor wing of the EUV distribution.

We compared finally the distribution of disc fractions as a function of age, calculated as the time at which the accretion rate drops below 10^{-11} $M_\odot$ yr^{-1} in our population synthesis with the observed distribution of disc fraction (Figure 4, black lines). As expected the EUV distribution fits perfectly, as we choose the parameter space in order to fit it for the median stellar mass and EUV ionizing field. The XEUV distribution is also very accurate in describing the observed star forming region population with the only constraint of an initial disc mass of 0.1 $M_\star$.

3.1 Mass dependent results

The results shown in the previous section assume a well-sampled IMF, which implies that objects at the lower end of the mass range are the most abundant (see Figure 1 panel a). However the sample of low accretors from Thanathibodee et al. (2023) includes only 24 objects with masses ranging between 0.1 and 1.39 $M_\odot$. The majority of which have masses between 0.5 and 0.6 $M_\odot$, resulting

Table 2. Parameters for the population synthesis calculations.

name	viscosity $\log_{10}(\alpha)$	r1 au	disc mass $M_\star$	stellar mass $M_\odot$	stellar flux $(\Phi_{EUV},\ L_X)$
EUV	eq. 19	eq. 19	eq. 19	Fig. 1 (panel a)	Fig. 1 (panel c)
XEUV	[-4, -2]	[10, 100]	0.1	Fig. 1 (panel a)	Fig. 1 (panel b)

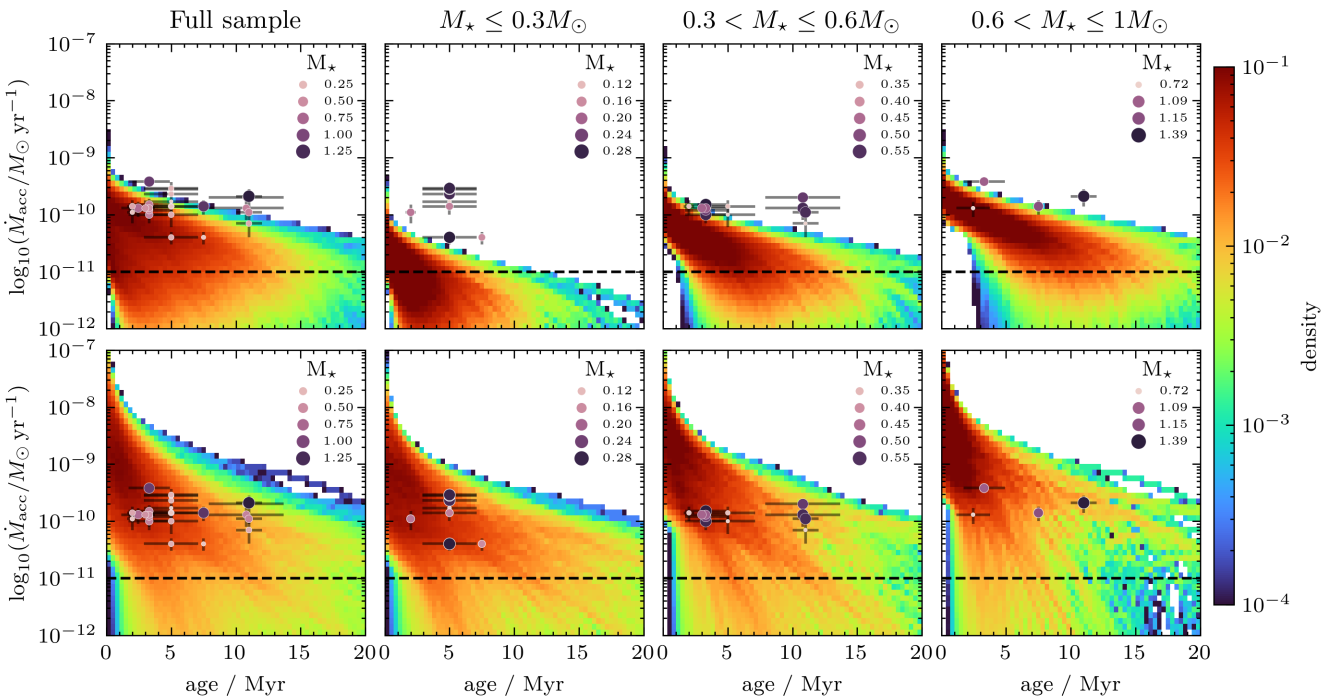

Figure 2. Synthetic populations showing the accretion rates as a function of age. The color mapping shows the probability of finding an object of a given age accreting at a given accretion rate (see text for details). Left panel: discs are dispersed by EUV photoevaporation; right panel: discs are dispersed by X-ray photoevaporation. The low-accretors population is overplotted with dots with variable size increasing by their stellar mass.

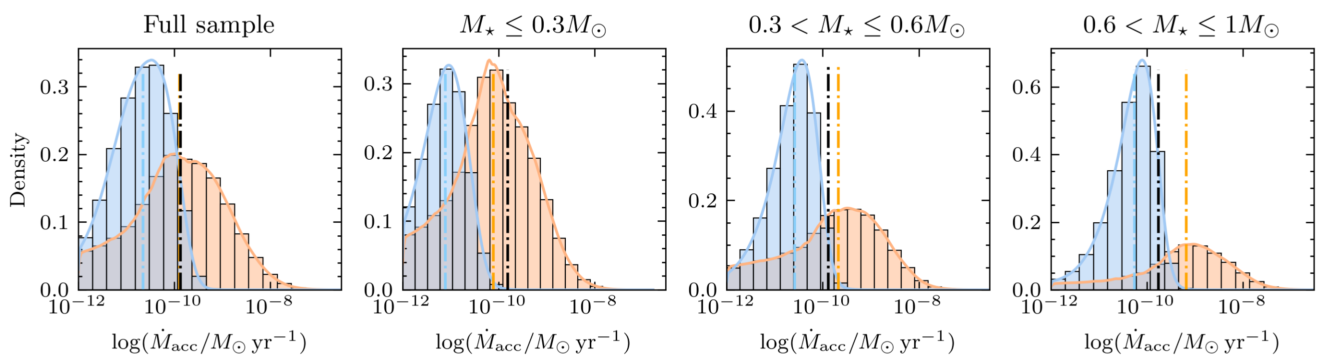

Figure 3. Histogram of the accretion rate density distribution in the EUV (blue) and XEUV (green) population synthesis. The KDE is overplotted with a blue and green solid line for the EUV and XEUV distributions respectively, and the median values are plotted with dotted-dashed lines. For direct comparison the median accretion rate of the low-accretors population is plotted with a black dotted-dashed line.

in a significant different stellar mass function with respect to the adopted IMF.

In Figure 4 we divided our sample in three different mass bins in order to understand the effect of stellar mass on the disc lifetime. In the top panel the XEUV profile shows little variation as a function of stellar mass, with a trend of decreasing lifetimes for increasing stellar masses, which is consistent with current observations reference?. In the bottom panel, the EUV profile shows a stronger dependence on the stellar mass, with an inverse trend of decreasing disc lifetime for smaller mass stars. The overall distribution in this case fits the observational data because of the adopted IMF, but it would over-

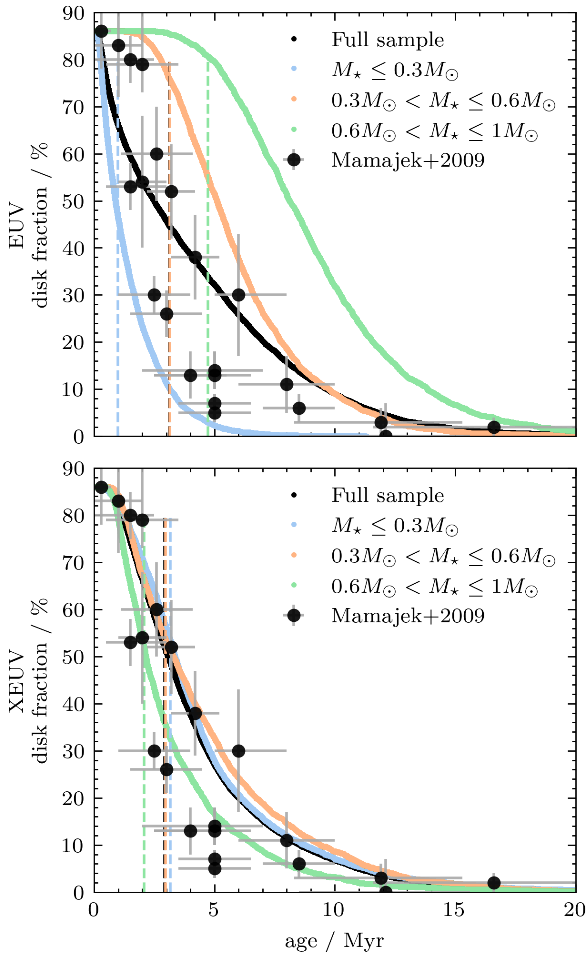

Figure 4. Disc fraction as a function of disc lifetime for the XEUV (top panel) and EUV (bottom panel) synthetic populations compared with the observational data from Mamajek (2009), divided in 3 stellar mass bins. The median disc lifetime are plotted with dashed vertical lines. The median disc life-time increases with stellar mass for the EUV models, while it decreases for the XEUV models.

predict the disc fractions for the stellar mass distribution studied in Thanathibodee et al. (2023).

3.2 Low-accretors variability

Fang et al. (2023) obtained the accretion rate of a large sample in Upper Sco adopting high-resolution optical spectra from Hα line profiles. Comparing their results with the ones measured for the same star forming region by Manara et al. (2020), fitting simultaneously the stellar photosphere and Balmer continuous emission, they find a large spread (see their Figure 29) going to more than one order of magnitude, especially for the population of low-accretors. Comparing the low accretors with the ones derived fitting the He I λ10830 line profiles in Thanathibodee et al. (2023) they found further differences in disc classification and accretion rates. This points towards a general difficulty in classifying low accretors based on line profiles, and their intrinsic variability that should be studied further.

4 CONCLUSIONS

We conducted a statistical study to examine the impact of different internal photoevaporation models on the physical limits observed in low-accretors.

Our main findings can be described as follows:

- Both internal EUV and X-ray photoevaporation can account for the observed accretion rates in the low-accretor sample.
- The constraints required by EUV internal photoevaporation to explain the observed disk lifetime are considerably more stringent than those of X-ray-driven disc evolution (see eq. 19).
- the low-accretors are part of the bulk distribution of X-ray driven photoevaporation (with the median accretion rate overlapping with the one from the sample from Thanathibodee et al. (2023)), while they represent the upper end of the EUV accretors (see Figures 2,3).
- The relationship between disk fraction and stellar mass exhibits a stronger dependence for EUV profiles, which contradicts the observed low-accretor population that shows similar accretion rates across a wide range of stellar masses.

In light of the results of the population synthesis models shown here, we conclude that the recent low-accretor observations point to X-ray photoevaporation as driving the final stages of disc dispersal.

ACKNOWLEDGEMENTS

DATA AVAILABILITY

The data for the population synthesis calculations is available at https://github.com/GiovanniPicogna/low-accretors

REFERENCES

Alcalá J. M., et al., 2017, A&A, 600, A20
Alexander R. D., Armitage P. J., 2007, MNRAS, 375, 500
Baraffe I., Chabrier G., Allard F., Hauschildt P. H., 1998, A&A, 337, 403
Ercolano B., Rosotti G., 2015, MNRAS, 450, 3008
Ercolano B., Picogna G., Monsch K., Drake J. J., Preibisch T., 2021, MNRAS, 508, 1675
Fang M., Pascucci I., Edwards S., Gorti U., Hillenbrand L. A., Carpenter J. M., 2023, ApJ, 945, 112
Feigelson E. D., et al., 2005, ApJS, 160, 379
Getman K. V., et al., 2005, ApJS, 160, 319
Getman K. V., Feigelson E. D., Garmire G. P., Broos P. S., Kuhn M. A., Preibisch T., Airapetian V. S., 2022, ApJ, 935, 43
Güdel M., et al., 2007, A&A, 468, 353
Kroupa P., 2001, MNRAS, 322, 231
Kuhn M. A., Hillenbrand L. A., 2019, ApJ, 883, 117
Lesur G., et al., 2022, arXiv e-prints, p. arXiv:2203.09821
Lynden-Bell D., Pringle J. E., 1974, MNRAS, 168, 603
Mamajek E. E., 2009, in Usuda T., Tamura M., Ishii M., eds, American Institute of Physics Conference Series Vol. 1158, Exoplanets and Disks: Their Formation and Diversity. pp 3–10 (arXiv:0906.5011), doi:10.1063/1.3215910
Manara C. F., et al., 2020, A&A, 639, A58
Monsch K., Ercolano B., Picogna G., Preibisch T., Rau M. M., 2019, MNRAS, 483, 3448
Pascucci I., Cabrit S., Edwards S., Gorti U., Gressel O., Suzuki T., 2022, arXiv e-prints, p. arXiv:2203.10068
Picogna G., Ercolano B., Owen J. E., Weber M. L., 2019, MNRAS, 487, 691
Picogna G., Ercolano B., Espaillat C. C., 2021, MNRAS, 508, 3611
Ribas Á., Merín B., Bouy H., Maud L. T., 2014, A&A, 561, A54
Skrutskie M. F., Dutkevitch D., Strom S. E., Edwards S., Strom K. M., Shure M. A., 1990, AJ, 99, 1187

Thanathibodee T., Calvet N., Hernández J., Maucó K., Briceño C., 2022, AJ, 163, 74
Thanathibodee T., Molina B., Serna J., Calvet N., Hernández J., Muzerolle J., Franco-Hernández R., 2023, ApJ, 944, 90

This paper has been typeset from a TEX/LATEX file prepared by the author.